PAPER

Check for updates

Vibrational band-structures caused by internal rotations of the boron Wankel rotor B$_{11}$$^-$

Yonghong Xu,[a] Huihui Wang,[ab] Yonggang Yang, [iD] *[ab] Changyong Li,[ab] Liantuan Xiao[ab] and Suotang Jia[ab]

Nuclear quantum effects are often neglected for systems without hydrogen atoms. However some planar boron rotors turn out to exhibit remarkable nuclear quantum effects. Recent experiment on infrared spectroscopy of B$_{13}$$^+$ shows unexpected spectral broadening which still awaits physical explanation. Here we present quantitative investigations of the vibrational energy levels of B$_{11}$$^-$ up to full dimension. A harmonic-bath averaged Hamiltonian suitable for planar boron rotors is constructed and used to predict typical types of vibrational states of B$_{11}$$^-$. Band structures caused by internal rotations are found for all the investigated vibrational states. The experimental phenomenon of spectral broadening is thus due to the band structures of the corresponding vibrational levels. The detailed information of the relevant vibrational states reported in the present work may provide valuable references for future investigations of high resolution spectroscopy of B$_{11}$$^-$.

1 Introduction

Molecular machines have been extensively investigated both experimentally and theoretically.[1–3] The development of boron-based molecular machines, in particular molecular motors,[4,5] is a promising research field. In 2010 the planar boron cluster B$_{19}$$^-$ (ref. 6 and 7) was reported to behave like a molecular Wankel motor, in which the intramolecular rotation between the inner and the outer rings is almost barrierless. Soon later similar internal rotations were reported in B$_{13}$$^+$,[8,9] B$_{20}$$^-$,[10] and B$_{18}$$^{2-}$.[11] The above mentioned boron clusters have roughly circular shapes thus the internal rotations are expected to be kind of smooth. It was then found that elongated boron clusters B$_{11}$$^-$ and B$_{15}$$^+$ also exhibit similar internal rotations.[12,13] The elongated boron clusters were described as nanoscale tank treads and the reason for their fluxionality were further addressed by investigations on B$_{10}$C.[14] Recently the transition-metal-doped boron cluster NiB$_{11}$$^-$ was also reported to exhibit internal rotation between its inner B$_3$ ring and the outer B$_8$ ring.[15] In general the wide availability of boron-based molecular Wankel motors profits from the fact that most medium-sized boron clusters are planar or quasi-planar.[16,17] The fluxionality of strong covalently bonded molecules such as the boron clusters was counterintuitive, but it was rationalized as a consequence of delocalized chemical bondings.[4] A sufficiently large

outer ring is important for such kind of internal rotations of boron clusters.[5]

It should be noted that nuclear quantum effects are in general important for large amplitude motions[18] such as the internal rotations of boron clusters.[19–22] In 2017 a universal mechanism for the internal rotations of planar boron clusters B$_{11}$$^-$, B$_{13}$$^+$, B$_{15}$$^+$, and B$_{19}$$^-$ was proposed,[19] with explicit treatment of nuclear quantum effects. Accordingly the inner wheel of each boron cluster rotates with respect to its pseudo-rotating outer bearing.[19] Rigorous study of nuclear quantum effects in medium to large molecules is challenging,[23–26] in particular when there are large amplitude motions. For this purpose the reaction path/surface Hamiltonian which divides the system into a few large amplitude motions and many small amplitude harmonic vibrations is a good alternative.[27,28] For reference a simplified one-dimensional reaction path Hamiltonian has been adopted in ref. 19, neglecting all the normal modes perpendicular to the reaction path, to predict band structures for the rotational/pseudo-rotational energy levels of B$_{11}$$^-$, B$_{13}$$^+$, B$_{15}$$^+$, and B$_{19}$$^-$. The first experimental infrared spectroscopy of B$_{13}$$^+$ shows unexpected broadening of some absorption bands,[29] which is consistent with the picture of energy bands but different from isolated levels calculated by standard harmonic frequencies. To discover what is the possible reason behind the observed spectral broadening it is important to obtain the details of all the relevant vibrational levels with resolution up to internal rotations. For this purpose we need full dimensional treatment for the corresponding vibrational states which will deeply expand and improve the results and physical picture in ref. 19.

In the present work we will quantitatively investigate the vibrational energy bands of the planar boron rotor B$_{11}$$^-$ using the

[a]State Key Laboratory of Quantum Optics and Quantum Optics Devices, Institute of Laser Spectroscopy, Shanxi University, Taiyuan 030006, China. E-mail: ygyang@sxu.edu.cn

[b]Collaborative Innovation Center of Extreme Optics, Shanxi University, Taiyuan 030006, China

intrinsic reaction path Hamiltonian. The nuclear quantum effects will be included up to full dimension. The relation between the intrinsic reaction path and the adopted reaction path in ref. 19 will be elucidated. The theory and methods for the Hamiltonian and vibrational states are in Section 2. The results and discussions are in Section 3 and the conclusions in Section 4.

2 Theory and methods

2.1 The intrinsic reaction path and coordinates

The global minimum (GM) and transition state (TS) structures of B_{11}^- are obtained using Gaussian09 suit of programs[30] at the PBE0/6-311+G* level of theory.[31] All the subsequent *ab initio* calculations are performed at the same level. B_{11}^- is a planar rotor. Due to the indistinguishability of identical boron atoms, there are in total 11! = 39, 916, 800 equivalent GMs. The number of accessible GMs is 18 by only considering the in-plane soft mode motions. They are connected cyclically by 18 TSs according to the following reaction mechanism

$$\text{GM}_1 \overset{\text{TS}_{1,2}}{\rightleftharpoons} \text{GM}_2 \overset{\text{TS}_{2,3}}{\rightleftharpoons} \text{GM}_3 \ldots \text{GM}_{18} \overset{\text{TS}_{18,1}}{\rightleftharpoons} \text{GM}_1$$

To get more details of the reaction we first locate the reaction path by the IRC (intrinsic reaction coordinate) calculations[32] as implemented in Gaussian09. This will start with a TS and follow the steepest descent direction until finally reaching a GM. The reaction path can be mathematically defined by the structure $R_0(s)$ of B_{11}^- for each value of s. Here s is the intrinsic reaction coordinate which is a mass-weighted variable in units of $\sqrt{m_e} \cdot a_0$, where m_e is electron mass and a_0 is Bohr radius. Thus the potential energy curve along the reaction path is $V_0(s) = V[R_0(s)]$.

In ref. 19 the reaction path has been well approximated as the inner wheel (two inner atoms) rotating with respect to the outer bearing (namely the outer ring of nine atoms) accompanied by small amplitude reshaping of the outer bearing (known as pseudorotation[33]) to adapt to the inner wheel's rotation. In ref. 19 it was shown that the complete set of motions during this reaction (namely both the internal rotation and the pseudorotation) can be uniformly characterized by a single angle variable φ. Consequently either s or φ can be used as our reaction coordinate. The equivalence between s and φ will be discussed in Section 3.

An arbitrary structure of B_{11}^- can be characterized by a vector R with $3N = 33$ cartesian components for the coordinates of $N = 11$ atoms. First of all we need to define the coordinates of arbitrary structures using our reaction coordinate φ. To simplify the things we use the molecular fixed frame with the origin at the center of mass and the orientations of the xyz-axes along the three principal axes of the moment of inertia. Consequently the three dimensional translation is separated and the three dimensional global rotation can be separated within a good approximation.

To define the coordinates of an arbitrary structure R, we need another $3N - 7$ coordinates apart from φ. It is more convenient to use the corresponding mass-weighted coordinates $\tilde{R}$. There are $3N - 7$ vibrational motions perpendicular to the reaction path. For most of the processes which are of interest, the perpendicular vibrations have small amplitudes. Therefore it is convenient to introduce the normal modes. Specifically we need to define normal mode vectors $\hat{e}_k(\varphi)$ on each grid φ of the reaction path. Subsequently the corresponding normal mode coordinates Q_k can be defined.

For convenience we denote the unit vector for the reaction coordinate, namely the tangent of the reaction path, as $\hat{e}_{1(\varphi)}$. By definition we have

$$\hat{e}_1(\varphi) = N_1 \frac{\mathrm{d}\widetilde{R}_0(\varphi)}{\mathrm{d}\varphi} = -N_2 \frac{\partial V}{\partial \tilde{R}}\Big|_{\widetilde{R}_0}(\varphi), \tag{1}$$

where N_1 and N_2 are the corresponding normalization constants and $\sim$ means the corresponding mass-weighted coordinates. Here $V(R)$ is the full dimensional potential energy surface which does not need to be available. Actually we only need the force $-\frac{\partial V}{\partial R}$ and the Hessian matrix $\frac{\partial^2 V}{\partial R^2}$ on each point of the reaction path $R_0(\varphi)$ which can be routinely obtained by quantum chemistry calculations. Note we use simplified notations $-\frac{\partial V}{\partial R}$ and $\frac{\partial^2 V}{\partial R^2}$ for the force and Hessian matrix with corresponding components $\left(\frac{\partial V}{\partial R}\right)_i = \frac{\partial V}{\partial R_i}$ and $\left(\frac{\partial^2 V}{\partial R^2}\right)_{ij} = \frac{\partial^2 V}{\partial R_i \partial R_j}$. The perpendicular normal mode vectors are

$$\hat{e}_k(\varphi), k = 2, 3, \ldots, 3N - 6. \tag{2}$$

They are obtained by diagonalizing the projected Hessian matrix

$$(1 - P)\frac{\partial^2 V}{\partial \tilde{R}^2}\Big|_{\widetilde{R}_0(\varphi)}(1 - P) \tag{3}$$

with $P = \hat{e}_1(\varphi)\hat{e}_1^{\mathrm{T}}(\varphi) + P_{\mathrm{T}} + P_{\mathrm{R}}$. The three projection operators $\hat{e}_1(\varphi)\hat{e}_1^{\mathrm{T}}(\varphi)$, P_{T} and P_{R} project out the components of the reaction coordinate, translation, and global rotation, respectively.[27,28] The superscript T means transpose. In our molecular-fixed frame, an arbitrary structure R can be characterized as

$$\tilde{R} = \widetilde{R}_0(\varphi) + \sum_{k=2}^{3N-6} Q_k \hat{e}_k(\varphi). \tag{4}$$

Note all the $\tilde{R}$, $\widetilde{R}_0(\varphi)$ and Q_k are mass-weighted coordinates.

2.2 The reaction path Hamiltonian and vibrational states

The vibrational wavefunctions are

$$\psi_{n_1 n_2 \ldots n_{3N-6}}^{\mathrm{vib}}(\varphi, Q_2, Q_3, \ldots, Q_{3N-6}) \equiv \psi_n^{\mathrm{vib}}(\varphi, Q). \tag{5}$$

According to ref. 34, the $3N - 7$ perpendicular modes $Q_2, Q_3, \ldots, Q_{3N-6}$ form a harmonic bath which weakly affects the motions along the reaction coordinate φ. For convenience we define $n_b = (n_2, n_3, \ldots, n_{3N-6})$ thus $n = (n_1, n_b)$. Using similar adiabatic approximations in ref. 34 and 35, the wavefunctions are approximated as

$$\psi_n^{\text{vib}}(\varphi, \mathbf{Q}) = \psi_{n_1 n_b}^{\text{vib}}(\varphi, \mathbf{Q}) \approx \psi_{n_1 n_b}^{\text{RP}}(\varphi) \prod_{k=2}^{3N-6} \psi_{n_k}^{\text{HO}}(Q_k; \varphi), \quad (6)$$

where ";" implies parametrical dependence, namely $\psi_{n_k}^{\text{HO}}$ parametrically depends on φ. Here $\psi_{n_k}^{\text{HO}}(Q_k; \varphi)$ is the n_k-th eigenstate of the corresponding harmonic oscillator defined by

$$\left[-\frac{\hbar^2}{2} \frac{\partial^2}{\partial Q_k^2} + \frac{1}{2}\omega_k^2(\varphi) Q_k^2 \right] \psi_{n_k}^{\text{HO}}(Q_k; \varphi)$$
$$= \left(n_k + \frac{1}{2} \right) \hbar \omega_k(\varphi) \psi_{n_k}^{\text{HO}}(Q_k; \varphi), \quad (7)$$

where the frequency $\omega_k(\varphi)$ is also obtained by diagonalization of the projected Hessian matrix in eqn (3). Specifically the non-zero eigenvalues and corresponding eigenvectors of the projected Hessian matrix are $\omega_k^2(\varphi)$ and $\hat{e}_k(\varphi)$, respectively. With the ansatz of the wavefunctions the full dimensional Schrödinger equation

$$H^{\text{vib}}(\varphi, \mathbf{Q}) \psi_n^{\text{vib}}(\varphi, \mathbf{Q}) = E_n \psi_n^{\text{vib}}(\varphi, \mathbf{Q}) \quad (8)$$

can be approximated as a series of one dimensional equations

$$H_{n_b}^{\text{HBA}}(\varphi) \psi_{n_1 n_b}^{\text{RP}}(\varphi) = E_n \psi_{n_1 n_b}^{\text{RP}}(\varphi). \quad (9)$$

Here $H_{n_b}^{\text{HBA}}(\varphi)$ is the harmonic-bath averaged (HBA) Hamiltonian adapted from ref. 34 and 35

$$H_{n_b}^{\text{HBA}}(\varphi) = -\frac{\hbar^2}{2} \frac{\partial}{\partial \varphi} \frac{1}{I_{\text{eff}}(\varphi)} \frac{\partial}{\partial \varphi} + V_{n_b}^{\text{HBA}}(\varphi),$$
$$V_{n_b}^{\text{HBA}}(\varphi) = V_0(\varphi) + \Delta V(\varphi) + \sum_{k=2}^{3N-6} \left(n_k + \frac{1}{2} \right) \hbar \omega_k^{\text{eff}}(\varphi), \quad (10)$$

where the effective moment of inertia and harmonic frequencies are

$$I_{\text{eff}}(\varphi) = I_0 \left[1 + \Delta_1(\varphi) \right],$$
$$\omega_k^{\text{eff}}(\varphi) = \omega_k(\varphi) [1 + \Delta_k(\varphi)]. \quad (11)$$

Here I_0 is the moment of inertia associated with the coordinate φ, which is just the moment of inertia in ref. 19. The correction factors $\Delta_k(\varphi)$ for both $k = 1$ and $k = 2, \ldots, 3N - 6$ are uniformly expressed as

$$\Delta_k(\varphi) = \frac{\hbar}{I_0} \sum_{l=2}^{3N-6} (2n_l + 1)|B_{lk}(\varphi)|^2 / 2\omega_l(\varphi) \quad (12)$$

with mode-coupling parameters

$$B_{lk}(\varphi) = \frac{\partial \hat{e}_l(\varphi)}{\partial \varphi} \cdot \hat{e}_k(\varphi). \quad (13)$$

The additional potential energy is

$$\Delta V(\varphi) = -\frac{\hbar^2}{4I_0} \sum_{k,l=2}^{3N-6} |B_{lk}(\varphi)|^2. \quad (14)$$

The central approximation of the HBA Hamiltonian is the adiabatic separation of the full dimensional wavefunction in eqn (6). The adiabatic approximation will be questionable if the motions along the reaction coordinate(s) are not slow compared

to the perpendicular vibrations of normal modes. In this case it is not recommended to use the HBA Hamiltonian. Another condition which should be fulfilled is weak mode-coupling since the HBA Hamiltonian is truncated to the second order of the coupling parameters $B_{lk}(\varphi)$ according to ref. 34. In most cases we may use reaction coordinate(s) to characterise large amplitude motions. Large amplitude may corresponds to long period and thus implies relatively good adiabatic separation. On the other hand the couplings may be decreased with suitable definitions of reaction coordinate(s). For the present reaction of internal rotations of B_{11}^-, it is suitable to use the HBA Hamiltonian for vibrational analysis.

3 Results and discussions

3.1 The reaction path and the harmonic-bath averaged Hamiltonian

The intrinsic reaction path $\mathbf{R}_0(s)$ obtained from IRC calculations for one-step reaction $GM_{18} \rightleftharpoons GM_1$ is shown in Fig. 1a. Each point in Fig. 1a stands for a boron atom and different boron atoms for a given structure are distinguished by different color. The potential energy curve $V_0(s)$ along the reaction path is shown in Fig. 1b. To gain more insights into the reaction mechanism, the normal modes (from diagonalization of unprojected Hessian matrix) which correlate with motions along the reaction path are shown in Fig. 1c ($TS_{18,1}$) and Fig. 1d (GM_1). The corresponding normal mode is the one with the imaginary frequency for $TS_{18,1}$ and the lowest-frequency in-plane mode for GM_1. The rather good correlation between the IRC in Fig. 1a and a single normal mode imply weak couplings between the reaction coordinate and the perpendicular normal modes.

We define the molecule to be in the xy-plane. According to ref. 19 the structure of $TS_{1,2}$ can be obtained by rotating $TS_{18,1}$ around the z-axis by $20° + 180° = 200°$. In terms of the reaction
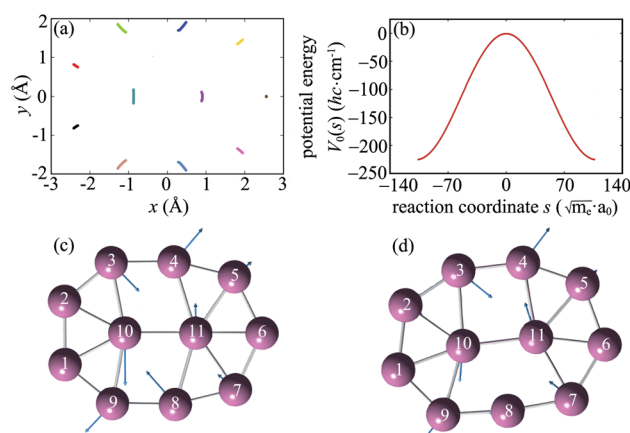
Fig. 1 The intrinsic reaction path and the associated normal modes. (a) The reaction path for the reaction $GM_{18} \rightleftharpoons TS_{18,1} \rightleftharpoons GM_1$ of B_{11}^- obtained by IRC calculations using Gaussian09. (b) The potential energy curve $V_0(s)$ along the reaction path. The corresponding domain for s is $[-107.92, 107.92] \sqrt{m_e} \cdot a_0$. (c) and (d) The normal modes of the $TS_{18,1}$ (c) and GM_1 (d) which correlate with the motions along the reaction path.

coordinate φ, from $TS_{18,1}$ to $TS_{1,2}$ corresponds to the internal rotation of the inner wheel with respect to the outer bearing around the z-axis by $\varphi = 20°$ accompanied by small amplitude motions of the outer bearing atoms (pseudorotations).

To be more specific, we use two angles φ_r and φ_b to characterize the rotations of the wheel and bearing, respectively. The corresponding moments of inertia for the wheel and bearing are I_r and I_b, respectively. The internal rotational angle is thus $\varphi = \varphi_r - \varphi_b$. For $\varphi = 20°$, we have $\varphi_r = \dfrac{I_b}{I_r + I_b} \times 20° = 19.32°$ and $\varphi_b = \dfrac{-I_r}{I_r + I_b} \times 20° = -0.68°$. Thus we can get $TS_{1,2}$ by first rotating the inner wheel of $TS_{18,1}$ around z-axis by $20°$ with corresponding small adaptions of outer bearing. Then perform a global rotation around z-axis by $-0.68°$. An equivalent way to obtain $TS_{1,2}$ from $TS_{18,1}$ is thus a simple global rotation around z-axis by $200° - 0.68° = 199.32°$. In this way we generate all the 18 TSs and obtain the full reaction path shown in Fig. 2a. The corresponding potential energy curve $V_0(s)$, or equivalently $V_0(\varphi)$, is shown in Fig. 2b with potential barrier $\Delta V_b = 225.65$ hc cm^{-1}.

In Fig. 2b we use two coordinates to characterize the same reaction. One is the intrinsic reaction coordinate s from *ab initio*

calculations. The other one is the internal rotation φ defined in ref. 19. It is straightforward to obtain the following relations:

$$s(TS_{i,i+1}) = 2i \cdot \Delta s, \; s(GM_i) = (2i - 1) \cdot \Delta s,$$
$$\varphi(TS_{i,i+1}) = 2i \cdot \Delta \varphi, \; \varphi(GM_i) = (2i - 1) \cdot \Delta \varphi, \quad (15)$$

where $\Delta s = 107.92 \sqrt{m_e} \cdot a_0$ and $\Delta \varphi = 10°$. Within a good approximation the two variables s and φ can be linearly transformed by $s = k\varphi$, with $k = \dfrac{\Delta s}{\Delta \varphi} = 618.35 \sqrt{m_e} \cdot a_0$. The details can be found from the two abscissas of Fig. 2b. By considering the zero order kinetic energy of both cases we have

$$T_0(s) = -\frac{\hbar^2}{2} \frac{\partial^2}{\partial s^2} = T_0(\varphi) = -\frac{\hbar^2}{2 I_0} \frac{\partial^2}{\partial \varphi^2}. \quad (16)$$

Since $\dfrac{\partial^2}{\partial s^2} = \dfrac{1}{k^2} \dfrac{\partial^2}{\partial \varphi^2}$ we can get the moment of inertia for φ as $I_0 = k^2 = 3.82 \times 10^5 m_e \cdot a_0^2$ which agrees well with the reported value of $3.74 \times 10^5 m_e \cdot a_0^2$ in ref. 19. The good agreement further confirms the equivalence between the two coordinates s and φ.

Up to now we have the complete information for the zero-order Hamiltonian $H_0(\varphi) = T_0(\varphi) + V_0(\varphi)$ up to an arbitrary energy reference which will be specified in Section 3.2. According to eqn (10), the zero-order Hamiltonian can be improved to the HBA Hamiltonian $H^{HBA}(\varphi)$ provided the zero-order moment of inertia and potential are replaced by $I_{eff}(\varphi)$ and $V^{HBA}(\varphi)$, respectively. The details of $V_{n_b}^{HBA}(\varphi)$ and $I_{eff}(\varphi)$ are shown in Fig. 3 for typical sets of quantum numbers n_b of the harmonic bath.

In the subsequent sections we selectively investigate three typical cases of the harmonic bath: the ground state, fundamental excitations, and combinational excitations. They can be identified by n_b which includes all the quantum numbers n_k for $k \geq 2$. Specifically we choose four cases including the ground state for $n_k = 0$, two fundamental excitations for $n_k = \delta_{k,2}$ and $n_k = \delta_{k,27}$, and one combinational excitation for $n_k = \delta_{k,2} + \delta_{k,27}$. Among all the 26 normal modes of the harmonic bath, the mode 2 and mode 27 are the lowest-frequency and the highest-frequency modes, respectively. Accordingly the HBA potential energy curves $V_{n_b}^{HBA}(\varphi)$ for the four cases are shown in Fig. 3a. They all have similar shapes as the zero-order potential $V_0(\varphi)$ in Fig. 1b and 2b. However they include corrections caused by couplings between any pair of coordinates, *cf.* eqn (10)–(14). An apparent consequence of these couplings is that the HBA potential barrier will be modified. The corresponding potential barriers are 221.90, 216.46, 240.39, and 234.92 hc cm^{-1} for $n_k = 0, \delta_{k,2}, \delta_{k,27}$, and $\delta_{k,2} + \delta_{k,27}$, respectively. Compared to the zero-order barrier of 225.65 hc cm^{-1}, the corresponding barriers are modified by -1.66%, -4.07%, 6.53%, and 4.11%, respectively. At first glance, the modifications of the HBA potential barriers are not large. However eigenenergies are in general rather sensitive to potential barriers. More details will be discussed in the subsequent sections.

Strictly speaking the effective moment of inertia $I_{eff}(\varphi)$ also depends on the set of quantum numbers n_b associated with the harmonic bath. However the dependence turns out to be negligible according to Fig. 3b. To simplify the notations we didn't explicitly write out the dependence of $I_{eff}(\varphi)$ on n_b. The differences of $I_{eff}(\varphi)$ between the four studied cases are not
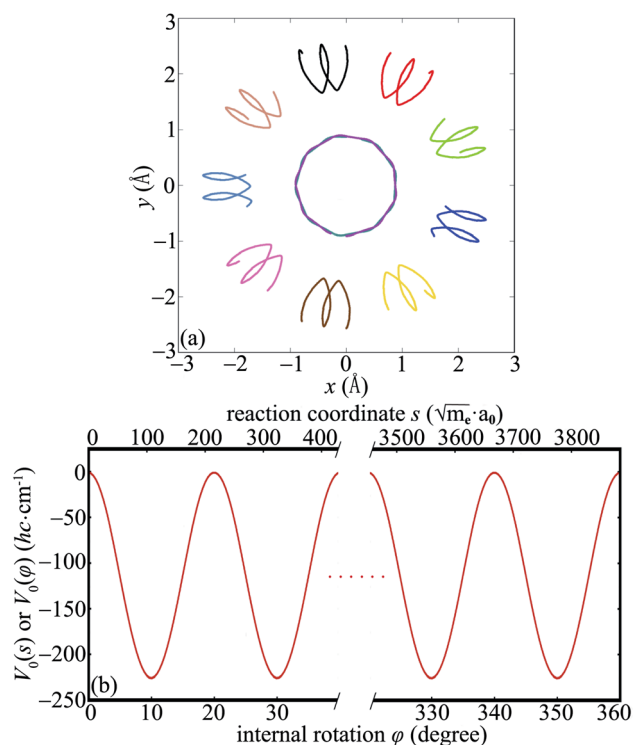
Fig. 2 The full cycle of the reaction path and the corresponding potential energy curve. (a) The reaction path for the reaction $TS_{18,1} \rightleftharpoons GM_1 \rightleftharpoons TS_{1,2} \rightleftharpoons GM_2 \ldots \rightleftharpoons GM_{18} \rightleftharpoons TS_{18,1}$. Note the initial $TS_{18,1}$ and the last $TS_{18,1}$ are different in the orientations by a small angle. This is because internal rotation of $\varphi = 360°$ is accompanied by a small-angle global rotation. (b) The corresponding potential energy curve along the reaction path. Two equivalent coordinates are indicated in the upper and lower abscissas for the intrinsic reaction coordinate s and the internal rotation φ, respectively.

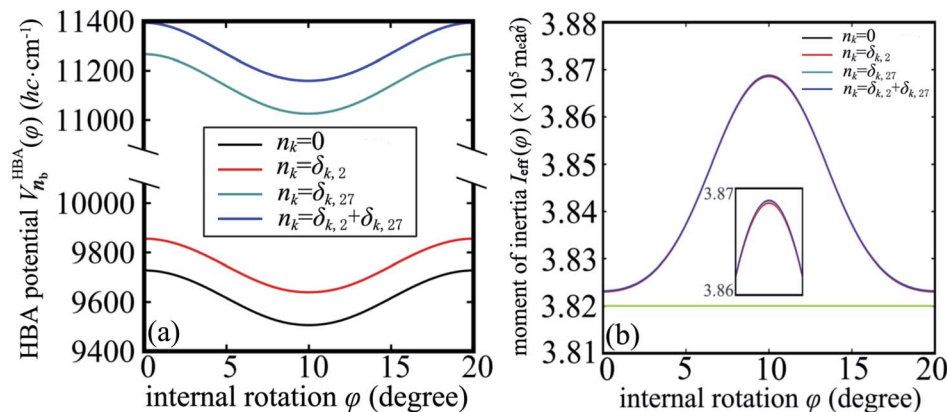**Fig. 3** (a) The potential $V_{n_b}^{\text{HBA}}(\varphi)$ for the harmonic–bath averaged Hamiltonian in eqn (10) with given quantum numbers n_b for the normal modes perpendicular to the reaction path. (b) The effective moment of inertia $I_{\text{eff}}(\varphi)$ for the internal rotation with given quantum numbers n_b. The green line indicates the zero-order moment of inertia I_0. Four different cases of n_b are investigated in both (a) and (b).

noticable on the graphic scale of Fig. 3b. An enlarged plot for $\varphi \in [8, 12]$ degrees is shown in the inset of Fig. 3b. Form the inset we can identify the extremely slight difference between $n_k = 0$ and $n_k = \delta_{k,27}$. The contributions to $I_{\text{eff}}(\varphi)$ from mode 2 is almost zero. Consequently the difference between $n_k = 0$ and $n_k = \delta_{k,2}$ (or between $n_k = \delta_{k,27}$ and $n_k = \delta_{k,2} + \delta_{k,27}$) is not noticable even in the enlarged inset. The value for the zero-order moment of inertia $I_0 = 3.82 \times 10^5 m_e \cdot a_0^2$ is indicated as a horizonal line. The value of $I_{\text{eff}}(\varphi)$ is always larger than I_0 for arbitrary φ due to non-negative characteristics of the factor $\Delta_1(\varphi)$ in eqn (12). In general the difference between $I_{\text{eff}}(\varphi)$ and I_0 is not large, which further validates eqn (10) for the present work.

3.2 The vibrational energy levels

Having the harmonic-bath averaged Hamiltonian $H_{n_b}^{\text{HBA}}(\varphi)$ at hand, we can calculate the corresponding eigenenergies of vibrational states with any quantum numbers $\mathbf{n}$. Accordingly the eigenenergies for the four cases studied in Fig. 3 (namely four sets of $n_b = \{n_k, k \geq 2\}$) are listed in Tables 1–4, respectively. In each table the lowest 36 eigenenergies are documented, which are labeled by the quantum number n_1 associated with the reaction coordinate φ. In general the 36 energy levels form two energy bands. For each of the investigated cases, the lowest energy band consists of 18 levels which are $0 \leq n_1 \leq 17$ with a band width less than $2hc$ cm^{-1}. While the second band for $18 \leq n_1 \leq 35$ has a band width more than $20hc$ cm^{-1}. Between the two energy bands there is a fairly large band gap of about $100hc$ cm^{-1}. Higher energy bands with levels above the barrier can also be calculated in the same spirit.

For detailed comparisons, the eigenenergies E_n calculated by three different models are reported in Tables 1–4. Apart from the HBA Hamiltonian, the other two are the harmonic approximation and the zero-order Hamiltonian, respectively. The harmonic energies are evaluated as $\sum_{k=1}^{3N-6} \left(n_k + \frac{1}{2} \right) \hbar \omega_k^{\text{GM}}$, where $\omega_k^{\text{GM}} = \omega_k(\varphi = 10°)$ is the corresponding harmonic frequency of the GM structure. Here n_1 is set to zero and ω_1 is the frequency of the mode shown in Fig. 1d. For convenient comparisons,

the zero-order Hamiltonian is defined as $H_0(\varphi) = T_0(\varphi) + V_0(\varphi) + \sum_{k=2}^{3N-6} \left(n_k + \frac{1}{2} \right) \hbar \omega_k^{\text{GM}}$ to be consistent with the other two models in energy reference. Note the Hamiltonian used in ref. 19 is $T_0(\varphi) + V_0(\varphi)$, which is essentially the same as $H_0(\varphi)$ except for different energy references.

The harmonic energy is listed in the second column of each table. The corresponding harmonic energy in Table 1, namely for the ground state, is the zero point energy. Apparently the zero point energy of $9580.6hc$ cm^{-1} is quite large. This large zero point energy is automatically included in all the reported values of eigenenergies in Tables 1–4 by the three models. The zero-order eigenenergies are essentially the same for all different cases of the harmonic bath, with detailed values listed in the third column of each table. The only difference between the third columns of any two tables is just a global shift of all energy levels. The ground state energy of $9581hc$ cm^{-1} is quite close to the harmonic value, which further confirms the good correlation between the normal mode in Fig. 1d and the internal rotation characterized in Fig. 1a and 2a. The eigenenergies obtained by diagonalization of the HBA Hamiltonian are listed in the fourth column of each table. In general the HBA energies are lower than the corresponding zero-order values. This is because the HBA Hamiltonian contains contributions from full dimensional motions of the molecule. Consequently the molecule has more freedom to relax, compared to the one-dimensional zero-order Hamiltonian. For example, the HBA ground state energy of $9569.66hc$ cm^{-1} is more stable than the corresponding zero-order level by $11.34hc$ cm^{-1}.

To get further details on how large the HBA Hamiltonian makes improvements to the eigenenergies compared to the zero-order Hamiltonian, the differences between the values of the corresponding eigenenergies E_n obtained by the HBA and the zero-order Hamiltonians are documented in Column 7 of each table. In general all the energy levels are further stabilized due to the improvements from the HBA Hamiltonian. Specifically the eigenenergies E_n are improved due to the HBA potential V^{HBA} and the moment of inertia I_{eff}. We further calculated

Table 1 Eigenenergies of the lowest two energy bands associated with the reaction coordinate φ for ground-state normal modes ($n_k = 0$ for $k \geq 2$)

Quantum number[a] n_1	Eigenenergy[b] E_n (hc cm^{-1})			HBA improvements[c] of E_n (hc cm^{-1})			Excitation energy $E_n - E_0$ (hc cm^{-1})	
	Harmonic	H_0	H^{HBA}	From V^{HBA}	From I_{eff}	From H^{HBA}	H_0	H^{HBA}
0	9580.60	9581.00	9569.66	−11.14	−0.20	−11.34	—	—
1, 2	—	9581.05	9569.69	−11.14	−0.22	−11.36	0.05	0.03
3, 4	—	9581.21	9569.83	−11.14	−0.25	−11.38	0.21	0.17
5, 6	—	9581.46	9570.07	−11.13	−0.27	−11.39	0.46	0.41
7, 8	—	9581.76	9570.35	−11.12	−0.29	−11.41	0.76	0.69
9, 10	—	9582.10	9570.68	−11.11	−0.32	−11.42	1.10	1.02
11, 12	—	9582.41	9570.98	−11.10	−0.34	−11.43	1.41	1.32
13, 14	—	9582.68	9571.24	−11.09	−0.35	−11.44	1.68	1.58
15, 16	—	9582.85	9571.41	−11.08	−0.36	−11.44	1.85	1.75
17	—	9582.91	9571.47	−11.08	−0.37	−11.44	1.91	1.81
18	—	9686.58	9673.75	−12.47	−0.36	−12.83	105.58	104.09
19, 20	—	9687.08	9674.25	−12.47	−0.37	−12.83	106.08	104.59
21, 22	—	9688.56	9675.72	−12.45	−0.39	−12.84	107.56	106.06
23, 24	—	9690.95	9678.10	−12.43	−0.43	−12.85	109.95	108.44
25, 26	—	9694.15	9681.28	−12.40	−0.48	−12.87	113.15	111.62
27, 28	—	9697.99	9685.10	−12.36	−0.53	−12.89	116.99	115.44
29, 30	—	9702.19	9689.28	−12.31	−0.60	−12.91	121.19	119.62
31, 32	—	9706.28	9693.35	−12.26	−0.67	−12.93	125.28	123.69
33, 34	—	9709.48	9696.54	−12.21	−0.73	−12.94	128.48	126.88
35	—	9710.73	9697.79	−12.19	−0.76	−12.94	129.73	128.13

[a] Eigenenergies associated with the reaction coordinate φ are labelled with quantum number n_1. The quantum number n_k ($k \geq 2$) is associated with the k-th normal mode. [b] Energies are calculated by three different models: the harmonic approximation, the zero-order Hamiltonian $H_0(\varphi)$ and the HBA Hamiltonian $H^{\text{HBA}}(\varphi)$ in eqn (10). [c] The improvements by $H^{\text{HBA}}(\varphi)$ with respect to $H_0(\varphi)$.

the improvements solely by V^{HBA} without I_{eff}, or solely by I_{eff} without V^{HBA}. The corresponding results are shown in Column 5 and Column 6, respectively. The improvements of E_n from I_{eff} almost have no differences between the four cases, which is consistent with Fig. 3b. The improvements in Column 7 of each table can be well approximated as sum of the corresponding values in Columns 5 and 6. This is because the two factors V^{HBA} and I_{eff} mainly affect potential energy and kinetic energy

Table 2 Same with Table 1 but for the fundamental excitation of mode 2 ($n_k = \delta_{k,2}$ for $k \geq 2$)

Quantum number n_1	Eigenenergy E_n (hc cm^{-1})			HBA improvements of E_n (hc cm^{-1})			Excitation energy $E_n - E_0$ (hc cm^{-1})	
	Harmonic	H_0	H^{HBA}	From V^{HBA}	From I_{eff}	From H^{HBA}	H_0	H^{HBA}
0	9729.77	9730.17	9701.25	−28.72	−0.20	−28.92	149.17	131.59
1, 2	—	9730.22	9701.29	−28.72	−0.22	−28.93	149.22	131.63
3, 4	—	9730.38	9701.44	−28.70	−0.25	−28.94	149.38	131.78
5, 6	—	9730.63	9701.69	−28.68	−0.27	−28.94	149.63	132.03
7, 8	—	9730.94	9702.00	−28.65	−0.29	−28.94	149.94	132.34
9, 10	—	9731.27	9702.34	−28.62	−0.32	−28.93	150.27	132.68
11, 12	—	9731.59	9702.66	−28.59	−0.34	−28.92	150.59	133.00
13, 14	—	9731.85	9702.94	−28.57	−0.35	−28.91	150.85	133.28
15, 16	—	9732.02	9703.12	−28.55	−0.36	−28.90	151.02	133.46
17	—	9732.08	9703.18	−28.55	−0.37	−28.90	151.08	133.52
18	—	9835.75	9803.16	−32.25	−0.36	−32.60	254.75	233.50
19, 20	—	9836.25	9803.66	−32.23	−0.37	−32.59	255.25	234.00
21, 22	—	9837.73	9805.16	−32.19	−0.39	−32.57	256.73	235.50
23, 24	—	9840.12	9807.58	−32.13	−0.43	−32.54	259.12	237.92
25, 26	—	9843.32	9810.82	−32.03	−0.48	−32.50	262.32	241.16
27, 28	—	9847.16	9814.72	−31.92	−0.53	−32.44	266.16	245.06
29, 30	—	9851.36	9819.00	−31.77	−0.60	−32.36	270.36	249.34
31, 32	—	9855.45	9823.19	−31.61	−0.67	−32.27	274.45	253.53
33, 34	—	9858.65	9826.48	−31.45	−0.73	−32.17	277.65	256.82
35	—	9859.90	9827.78	−31.38	−0.76	−32.12	278.90	258.12

Table 3 Same with Table 1 but for the fundamental excitation of mode 27 ($n_k = \delta_{k,27}$ for $k \geq 2$)

Quantum number n_1	Eigenenergy E_n ($hc\ \mathrm{cm}^{-1}$)			HBA improvements of E_n ($hc\ \mathrm{cm}^{-1}$)			Excitation energy $E_n - E_0$ ($hc\ \mathrm{cm}^{-1}$)	
	Harmonic	H_0	H^{HBA}	From V^{HBA}	From I_{eff}	From H^{HBA}	H_0	H^{HBA}
0	11 096.46	11 096.85	11 090.25	−6.39	−0.20	−6.60	1515.86	1520.59
1, 2	—	11 096.91	11 090.28	−6.40	−0.23	−6.63	1515.91	1520.62
3, 4	—	11 097.07	11 090.40	−6.42	−0.25	−6.67	1516.07	1520.74
5, 6	—	11 097.32	11 090.59	−6.44	−0.27	−6.72	1516.32	1520.93
7, 8	—	11 097.62	11 090.84	−6.48	−0.30	−6.78	1516.62	1521.18
9, 10	—	11 097.95	11 091.12	−6.51	−0.32	−6.84	1516.95	1521.46
11, 12	—	11 098.27	11 091.38	−6.55	−0.34	−6.89	1517.27	1521.72
13, 14	—	11 098.54	11 091.60	−6.58	−0.35	−6.94	1517.54	1521.94
15, 16	—	11 098.71	11 091.74	−6.60	−0.36	−6.96	1517.71	1522.08
17	—	11 098.77	11 091.79	−6.61	−0.37	−6.98	1517.77	1522.13
18	—	11 202.44	11 199.17	−2.87	−0.37	−3.27	1621.44	1629.51
19, 20	—	11 202.94	11 199.63	−2.90	−0.37	−3.31	1621.94	1629.97
21, 22	—	11 204.41	11 200.98	−3.00	−0.39	−3.43	1623.41	1631.32
23, 24	—	11 206.80	11 203.17	−3.17	−0.43	−3.64	1625.80	1633.51
25, 26	—	11 210.00	11 206.07	−3.41	−0.48	−3.93	1629.00	1636.41
27, 28	—	11 213.84	11 209.53	−3.74	−0.54	−4.32	1632.84	1639.87
29, 30	—	11 218.05	11 213.24	−4.17	−0.61	−4.81	1637.05	1643.58
31, 32	—	11 222.14	11 216.75	−4.68	−0.68	−5.39	1641.14	1647.09
33, 34	—	11 225.33	11 219.40	−5.17	−0.74	−5.93	1644.33	1649.74
35	—	11 226.59	11 220.41	−5.39	−0.76	−6.18	1645.59	1650.75

separately. Since I_{eff} is larger than I_0, *cf.* Fig. 3b or eqn (11), the kinetic energy from the HBA Hamiltonian is lower than the zero-order case. Concerning the potential energy, the difference between V^{HBA} and V_0 contains two terms according to eqn (10). One term is $\Delta V(\varphi)$ in eqn (14). According to eqn (14), $\Delta V(\varphi)$ is negative and does not depends on quantum numbers n_b of normal modes. For each of the reported energy levels the mean value of $\Delta V(\varphi)$ is about $-100hc\ \mathrm{cm}^{-1}$. The other term is the average energy of the 26 normal modes in terms of effective harmonic frequencies $\omega_k^{\mathrm{eff}}(\varphi)$. According to eqn (11) each effective frequency $\omega_k^{\mathrm{eff}}(\varphi)$ is larger than the original frequency $\omega_k(\varphi)$. Consequently the contribution of this term to the total eigenenergy E_n is larger than the corresponding zero-order case. The sum of the above two potential energy terms leads to negative contributions for E_n (compared to zero-order) as shown in Column 5 of each table.

Table 4 Same with Table 1 but for the combinational excitation of modes 2 and 27 ($n_k = \delta_{k,2} + \delta_{k,27}$ for $k \geq 2$)

Quantum number n_1	Eigenenergy E_n ($hc\ \mathrm{cm}^{-1}$)			HBA improvements of E_n ($hc\ \mathrm{cm}^{-1}$)			Excitation energy $E_n - E_0$ ($hc\ \mathrm{cm}^{-1}$)	
	Harmonic	H_0	H^{HBA}	From V^{HBA}	From I_{eff}	From H^{HBA}	H_0	H^{HBA}
0	11 245.63	11 246.03	11 221.88	−23.94	−0.20	−24.14	1665.03	1652.22
1, 2	—	11 246.08	11 221.91	−23.94	−0.23	−24.17	1665.08	1652.25
3, 4	—	11 246.24	11 222.04	−23.95	−0.25	−24.20	1665.24	1652.38
5, 6	—	11 246.49	11 222.25	−23.97	−0.27	−24.24	1665.49	1652.59
7, 8	—	11 246.79	11 222.52	−23.98	−0.30	−24.28	1665.79	1652.86
9, 10	—	11 247.13	11 222.81	−24.00	−0.32	−24.32	1666.13	1653.15
11, 12	—	11 247.44	11 223.08	−24.02	−0.34	−24.36	1666.44	1653.42
13, 14	—	11 247.71	11 223.32	−24.04	−0.35	−24.39	1666.71	1653.66
15, 16	—	11 247.88	11 223.47	−24.05	−0.36	−24.41	1666.88	1653.81
17	—	11 247.94	11 223.52	−24.05	−0.37	−24.42	1666.94	1653.86
18	—	11 351.61	11 328.66	−22.56	−0.37	−22.95	1770.61	1759.00
19, 20	—	11 352.11	11 329.13	−22.59	−0.37	−22.99	1771.11	1759.47
21, 22	—	11 353.58	11 330.50	−22.66	−0.39	−23.08	1772.58	1760.84
23, 24	—	11 355.97	11 332.73	−22.78	−0.43	−23.24	1774.97	1763.07
25, 26	—	11 359.17	11 335.70	−22.97	−0.48	−23.47	1778.17	1766.04
27, 28	—	11 363.01	11 339.23	−23.22	−0.54	−23.79	1782.01	1769.57
29, 30	—	11 367.22	11 343.03	−23.56	−0.61	−24.19	1786.22	1773.37
31, 32	—	11 371.31	11 346.65	−23.97	−0.68	−24.67	1790.31	1776.99
33, 34	—	11 374.50	11 349.38	−24.37	−0.74	−25.12	1793.50	1779.72
35	—	11 375.76	11 350.43	−24.55	−0.76	−25.33	1794.76	1780.77

For possible comparisons with high-resolution experiments which may be measurable in the future, we further calculated the excitation energy $E_n - E_0$ for each of the investigated states. The corresponding values are documented in the last two columns of Tables 1–4 for zero-order and HBA models, respectively. For the ground state harmonic bath (Table 1) all the excitation energies from HBA Hamiltonian are slightly redshifted compared to zero-order case. Similarly all the HBA excitation energies are redshifted by about $20hc$ cm^{-1} in Table 2 (fundamental excitation of mode 2). However, for the fundamental excitation of mode 27 in Table 3, all the HBA excitation energies are blueshifted by several wavenumbers. Then the combinational excitation case in Table 4 also exhibits redshifts for all the HBA excitation energies due to the competition between mode 2 and mode 27.

To deeply investigate the properties of the energy bands, we can arrange the four studied cases in terms of barrier heights. Consequently we have Tables 2, 1, 4, and 3 with barrier heights in ascending order: 216.46, 221.90, 234.92, and 240.39hc cm^{-1}, respectively. Note we only focus on results of the HBA model for the time being. In this order the band widths of the lowest energy band are 1.93, 1.81, 1.64, and 1.54hc cm^{-1}, respectively. The band widths of the second energy band are 24.62, 24.04, 21.77, and 21.24hc cm^{-1}, respectively. Clearly the band width decreases when the barrier height increases, for both the lowest and the second energy bands. While the corresponding band gaps are 99.98, 102.28, 105.14, and 107.38hc cm^{-1}, respectively. The band gap increases when the barrier height increases. Since the differences between the effective moment of inertia are negligible, *cf.* Fig. 3b, the behavior of the band structures can be predicted and explained purely in terms of the barrier heights. The band gap can be approximately estimated as the fundamental excitation energy for an isolated potential well. Higher barrier leads to larger curvature of the potential well, which in turn has higher fundamental transition frequency. The band width is determined by tunnelling between neighbouring potential wells. Higher barrier leads to smaller tunnelling probability and consequently to narrower band width. For infinitely high barrier, tunnelling is prohibited thus the band width would be zero. Harmonic approximation corresponds to the case of infinitely high barrier so that the system would be located in a single potential well. In this case the unexpected spectral broadening observed in ref. 29 would disappear. However in reality the barrier is rather low. Consequently tunnelling between neighboring potential wells gives rise to fairly large tunnelling splittings which appear as band widths of vibrational levels. The phenomenon happens essentially in all the relevant vibrational levels, which leads to spectral broadening of the infrared spectra.

4 Conclusions

Nuclear quantum effects beyond harmonic approximation are important for boron Wankel rotors. A simplified one-dimensional model in ref. 19 predicts rotational/pseudo-rotational energy bands which triggers full dimensional quantum mechanical investigations to unravel the origin of the line broadening of recent infrared spectra.[29] In the present work we construct a practical harmonic-bath averaged Hamiltonian and calculate the eigenenergies of relevant vibrational states, starting from a full dimensional reaction path Hamiltonian using the cyclic intrinsic reaction coordinate. Typical vibrational states including cases of ground-state, fundamental, and combinational excitations of normal modes are investigated. All the calculated energy levels associated with the internal rotations of $B_{11}{}^-$ are improved compared to the one dimensional results in ref. 19 for the case of ground-state normal modes. The present work further includes analysis of typical excitations of normal modes. Different mode excitations are found to have negligible effects on the moment of inertia but do have some influence on the effective potential for the internal rotation. The height of the potential barrier is modified due to mode excitations which in turn changes the details of the energy bands. With increasing barrier the band width decreases and the band gap increases. For all the investigated vibrational states, the lowest and second energy bands have band widths ranging from 1.5 to 2.0hc cm^{-1} and from 21 to 25hc cm^{-1}, respectively. The corresponding band gaps ranges from 99 to 108hc cm^{-1}. We find that the observed phenomenon of spectral broadening in ref. 29 is due to the band structures of the vibrational levels of boron rotors. The observed spectral broadening will be narrowed provided all the ^{10}B atoms are substituted by ^{11}B atoms. Heavier boron atoms lead to smaller tunnelling probability and consequently to a narrower band width for each energy band. This isotope effects can be observed by infrared experiments provided the resolution is sufficiently high. The reported quantitative energy levels in this paper may provide valuable references for future related investigations of high resolution spectroscopy. In addition the present method can be applied to study vibrational states of other medium to large molecules which may be rather challenging for typical full dimensional quantum dynamics calculations.

Author contributions

Y. Y. provided the concept and the model; Y. X. carried out the calculations, obtained the results, and prepared the figures; Y. Y. wrote the first draft of the manuscript. All coauthors contributed to the final version of the manuscript.

Conflicts of interest

There are no conflicts of interest to declare.

Acknowledgements

References

1 B. A. Feringa, *Angew. Chem., Int. Ed.*, 2017, **56**, 11060–11078.

2 J.-P. Sauvage, *Angew. Chem., Int. Ed.*, 2017, **56**, 11080–11093.

3 J. F. Stoddart, *Angew. Chem., Int. Ed.*, 2017, **56**, 11094–11125.

4 S. Pan, J. Barroso, S. Jalife, T. Heine, K. R. Asmis and G. Merino, *Acc. Chem. Res.*, 2019, **52**, 2732–2744.

5 S. Jalife, L. Liu, S. Pan, J. L. Cabellos, E. Osorio, C. Lu, T. Heine, K. J. Donald and G. Merino, *Nanoscale*, 2016, **8**, 17639–17644.

6 W. Huang, A. P. Sergeeva, H.-J. Zhai, B. B. Averkiev, L.-S. Wang and A. I. Boldyrev, *Nat. Chem.*, 2010, **2**, 202–206.

7 J. O. C. Jiménez-Halla, R. Islas, T. Heine and G. Merino, *Angew. Chem., Int. Ed.*, 2010, **49**, 5668–5671.

8 G. Martinez-Guajardo, A. P. Sergeeva, A. I. Boldyrev, T. Heine, J. M. Ugalde and G. Merino, *Chem. Commun.*, 2011, **47**, 6242–6244.

9 J. Zhang, A. P. Sergeeva, M. Sparta and A. N. Alexandrova, *Angew. Chem., Int. Ed.*, 2012, **51**, 8512–8515.

10 T. B. Tai, A. Ceulemans and M. T. Nguyen, *Chem.–Eur. J.*, 2012, **18**, 4510–4512.

11 D. Moreno, S. Pan, L. L. Zeonjuk, R. Islas, E. Osorio, G. Martinez-Guajardo, P. K. Chattaraj, T. Heine and G. Merino, *Chem. Commun.*, 2014, **50**, 8140–8143.

12 Y.-J. Wang, X.-Y. Zhao, Q. Chen, H.-J. Zhai and S.-D. Li, *Nanoscale*, 2015, **7**, 16054–16060.

13 Y.-J. Wang, X.-R. You, Q. Chen, L.-Y. Feng, K. Wang, T. Ou, X.-Y. Zhao, H.-J. Zhai and S.-D. Li, *Phys. Chem. Chem. Phys.*, 2016, **18**, 15774–15782.

14 Y.-J. Wang, J.-C. Guo and H.-J. Zhai, *Nanoscale*, 2017, **9**, 9310–9316.

15 X.-Y. Zhao, X.-M. Luo, X.-X. Tian, H.-G. Lu and S.-D. Li, *J. Cluster Sci.*, 2019, **30**, 115–121.

16 W.-L. Li, X. Chen, T. Jian, T.-T. Chen, J. Li and L.-S. Wang, *Nat. Rev. Chem.*, 2017, **1**, 0071.

17 Q. Chen, T.-T. Chen, H.-R. Li, X.-Y. Zhao, W.-J. Chen, H.-J. Zhai, S.-D. Li and L.-S. Wang, *Nanoscale*, 2019, **11**, 9698–9704.

18 E. T. Markland and M. Ceriotti, *Nat. Rev. Chem.*, 2018, **2**, 0109.

19 Y. Yang, D. Jia, Y.-J. Wang, H.-J. Zhai, Y. Man and S.-D. Li, *Nanoscale*, 2017, **9**, 1443–1448.

20 D. Jia, J. Manz and Y. Yang, *AIP Adv.*, 2018, **8**, 045222.

21 T. Grohmann and J. Manz, *Mol. Phys.*, 2018, **116**, 2538–2555.

22 T. Grohmann, D. Haase, D. Jia, J. Manz and Y. Yang, *J. Chem. Phys.*, 2018, **149**, 184302.

23 Y. Yang and O. Kühn, *Mol. Phys.*, 2008, **106**, 2445–2457.

24 V. May and O. Kühn, *Charge and Energy Transfer Dynamics in Molecular Systems*, WILEY-VCH Verlag GmbH & Co. KGaA, Weinheim, 3rd edn, 2011.

25 *Molecular Quantum Dynamics*, ed. F. Gatti, Springer-Verlag, Heidelberg, 2014.

26 C. Fábri, R. Marquardt, A. G. Császár and M. Quack, *J. Chem. Phys.*, 2019, **150**, 014102.

27 W. H. Miller, N. C. Handy and J. E. Adams, *J. Chem. Phys.*, 1980, **72**, 99–112.

28 T. Carrington Jr and W. H. Miller, *J. Chem. Phys.*, 1984, **81**, 3942–3950.

29 M. R. Fagiani, X. Song, P. Petkov, S. Debnath, S. Gewinner, W. Schöllkopf, T. Heine, A. Fielicke and K. R. Asmis, *Angew. Chem., Int. Ed.*, 2017, **56**, 501–504.

30 M. J. Frisch, G. W. Trucks and H. B. Schlegel, *et al.*, *Gaussian 09, Revision B.01*, Gaussian Inc., Wallingford, CT, 2009.

31 C. Adamo and V. Barone, *J. Chem. Phys.*, 1999, **110**, 6158–6170.

32 K. Fukui, *Acc. Chem. Res.*, 1981, **14**, 471–476.

33 J. Manz, *J. Am. Chem. Soc.*, 1980, **102**, 1801–1806.

34 Y. Yang and M. Meuwly, *J. Chem. Phys.*, 2010, **133**, 064503.

35 Y. Yang, X. Liu, M. Meuwly, L. Xiao and S. Jia, *J. Phys. Chem. A*, 2012, **116**, 11134–11139.